

Received January 27, 2020, accepted February 24, 2020, date of publication March 12, 2020, date of current version March 20, 2020.

Digital Object Identifier 10.1109/ACCESS.2020.2980229

Wave Excitation Force Estimation Using an Electrical-Based Extended Kalman Filter for Point Absorber Wave Energy Converters

MOHAMMED JAMA¹, ADDY WAHYUDIE², AND
SAAD MEKHILEF^{3,4}, (Senior Member, IEEE)

¹Emirates Centre of Energy and Environment Research (ECEER), United Arab Emirates University, Al Ain 15551, United Arab Emirates

²Department of Electrical Engineering, United Arab Emirates University, Al Ain 15551, United Arab Emirates

³Power Electronics and Renewable Energy Research Laboratory (PEARL), Department of Electrical Engineering, University of Malaya, Kuala Lumpur 50603, Malaysia

⁴School of Software and Electrical Engineering, Swinburne University of Technology, Melbourne, VIC 3122, Australia

Corresponding author: Addy Wahyudie (addy.w@uaeu.ac.ae)

This work was supported in part by the Joint Research Program between UAE University and Asian Universities Alliance (AUA) under Grant 31R169.

ABSTRACT Accurate real-time knowledge of the wave excitation force affecting a wave energy converter (WEC) – either through measurement or by estimation – is crucial for implementing effective control strategies that ensure optimum power absorption, system reliability, and durability. The estimation of the excitation force using other readily available measurements is deemed a cost-effective solution given the technical difficulties associated with directly measuring the excitation force on the WEC's floater hull. In this study, an electrical-based extended Kalman filter (E-EKF) estimator for estimating the wave excitation force, floater's heave displacement, and velocity is proposed. The estimator is derived using a holistic nonlinear wave-to-wire model of a direct-drive heaving WEC. A continuous and differentiable approximation of the well-known Tustin friction model is utilized to incorporate the friction force model into the estimator. The proposed E-EKF estimator requires only the measurement of the three-phase permanent magnet linear generator stator currents using current transducers. A practical approach is provided to overcome the need for measuring the wave surface elevation and velocity. Simulations are conducted to assess the goodness of the proposed E-EKF under various sea-state conditions, modeling mismatches, and electric loading scenarios. For the sake of comparison, the performance of the E-EKF estimator is measured against mechanical-based extended Kalman filter and linearized mechanical Kalman filter estimators. The E-EKF estimator exhibits superior performance in terms of nearly all performance metrics, with an excitation energy percentage error score not exceeding 9 %, while being immune to measurement noise.

INDEX TERMS Excitation force, extended Kalman filter, nonlinear model, permanent magnet linear generator, point absorber, state estimator, wave energy converter, wave-to-wire model.

I. INTRODUCTION

The wave excitation force is a function of incoming wave characteristics (i.e., wave amplitude, frequency, and direction) and the intercepting body geometry. The excitation force is made of two components: the Froude–Krylov force, which is defined as the dynamic pressure field exerted by the undisturbed waves integrated over the wetted surface area

The associate editor coordinating the review of this manuscript and approving it for publication was Ramesh Babu N¹.

of the intercepting body (i.e., floater), and the diffraction force, which is defined as the pressure field resulting from diffracted waves integrated over the wetted surface area [1]. If the wave energy converter (WEC) floater is small in size compared to the wavelength of the incoming wave, the Froude–Krylov force component dominates the wave excitation force. To implement real-time control strategies to control WECs, the wave excitation force needs to be estimated or measured at every time instant. For the excitation force estimation, the linear and causal relationship between the wave

elevation and the wave excitation force is approximated by frequency response functions (FRFs) [2]. Numerical tools are used to solve the wave excitation problem for various wave frequencies, and frequency-domain regression techniques are deployed to determine the FRFs [3]. Furthermore, in this method, it is assumed that the wave propagation in space and time is a linear system (i.e., linear wave theory) and the originally noncausal relation between the wave excitation force and the incoming wave elevation is also causalized. Therefore, any real-time calculation of the excitation force using the wave elevation time series is only an approximation of what is actually experienced by the floater [4]. One more issue in this method is the need to conduct the wave elevation measurement upstream of the location of the WEC as the wave elevation measurement is not easily attainable in the vicinity of the WEC – especially for multidirectional sea waves – which makes implementing this method in real time even more complex. Another method to obtain the excitation force values in real time is to measure the hydrodynamic pressure applied at the wetted surface area of the floater [1].

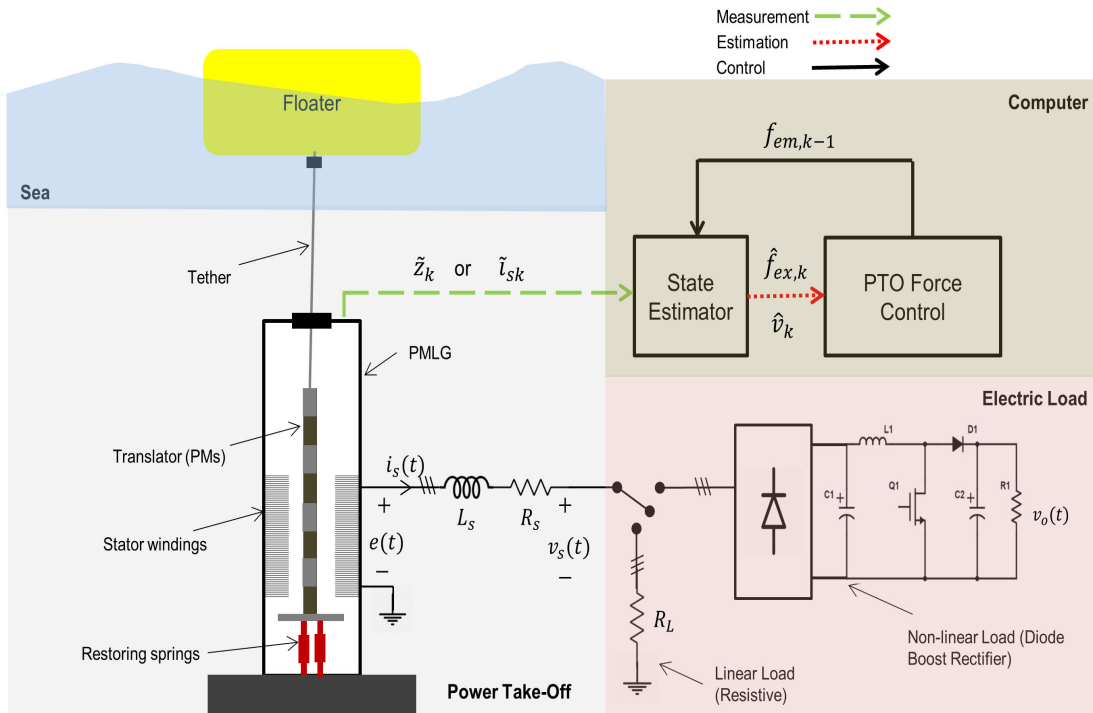
Recently, several wave excitation force estimation techniques have been reported in the literature. A linear state observer to estimate the wave excitation torque of the WaveStar WEC is presented in [5]. The linear observer is part of an overall servo-tracking control problem in which the floater velocity is manipulated to track a predetermined reference velocity using the estimated excitation torque. Although the control strategy has been tested experimentally, a simplified WEC model has been used to construct the observer, i.e., nonlinear dynamics is not involved. In [6], an extended Kalman filter is used to estimate the wave excitation forces using measurements of the hydrodynamic pressure at various points of the floater wetted surface along with the floater's position. No control force is applied, i.e., the floater is freely oscillating. The proposed estimator requires numerous pressure transducers, which might exacerbate the computational complexity of the estimator. An estimation technique based on floater hull pressure measurements along with the floater's heave displacement and acceleration measurements is introduced in [7]. The reported method lacks an explicit mechanism to handle measurement noise. A linear Kalman filter estimator coupled with a random walk model is discussed in [8]. The Kalman filter is based on a linear WEC model, in which the floater motion states (i.e., position and velocity) along with the power take-off (PTO) control force measurement via a load cell is fed to the estimator. The estimator goodness is verified experimentally. The same authors discussed a receding horizon estimator using the same set of measurement signals. A slightly different wave excitation force estimator that utilizes a linear Kalman filter with a harmonic oscillator model synthesizing the excitation force is reported in [9]. A similar approach was extended to collectively estimate the wave excitation force affecting each single WEC device in an array of WECs [10]. An unknown input observer (UIO) is proposed in [11] to estimate the excitation force and the floater velocity using measurements of the

displacement and PTO current. The method utilizes a simplified linear model of the WEC with frequency-independent hydrodynamic functions. The observer gain is determined using an H_∞ optimization technique. The method generally produced satisfactory results in nominal condition; however, the performance deteriorated significantly when parameter perturbations were applied. Another UIO technique, in which only the position measurement is required, has been reported in [7]. The method uses a linearized model of the WEC, and a linear matrix inequality (LMI) formulation of the H_∞ optimization technique – previously deployed in [11] – is used in an attempt to minimize the effect of the derivative operator on the estimation accuracy. The method performs well for sea states with large amplitudes and low frequencies, whereas it has produced significantly higher estimation errors for waves with low amplitudes and high frequencies.

In this work, a nonlinear state estimator based on an extended Kalman filtering approach to estimate the wave excitation force, the floater's heave displacement, and velocity is proposed. A comprehensive nonlinear wave-to-wire model of the WEC is deployed that includes the viscous drag force and the friction force. The proposed estimator requires only the real-time measurement of the PTO three-phase stator currents, which makes the technique easy to implement. Moreover, the absence of mechanical sensors improves the implementability of the proposed estimation technique. Also, owing to their confined physical footprint, absence of moving parts, and relatively low cost, electric transducers are more suitable for hardware redundancy, which further enhances the system reliability. The introduced estimation technique inherently and effectively handles measurement noise associated with current transducers (CTs). The highly nonlinear friction force that might result from the movement of the system parts against each other is modeled using a continuous and differentiable version of the well-known Coulomb friction model with viscous and Stribeck components. Similar to the method in [8], the wave excitation force is modeled as a random walk process with a drift. The viscous drag force is modeled using Morison's equation, in which the real-time water surface velocity is computed without the need for wave elevation measurement. The goodness of the state estimators under investigation has been assessed through simulations as part of a holistic wave-to-wire WEC system. That includes analyzing the effect of sea wave characteristics, parametric uncertainties, measurement noise, and electric loading scenarios. The paper is organized as follows: Section II discusses the wave-to-wire model of the point absorber WEC. The state estimators are derived in Section III. The proposed estimators are assessed via computer simulations in Section IV. Finally, conclusions are drawn in Section V.

II. POINT ABSORBER WEC MODEL

In this study, a direct-drive-based semi-submerged point absorber WEC is investigated, as shown in Fig. 1. The forces acting on the point absorber oscillating body (floater) in the heave degree of freedom of motion can be expressed using


FIGURE 1. Point absorber WEC system schematic.

Newton's second law of motion [12] as

$$f_h(t) + f_{pto}(t) = ma(t), \quad (1)$$

where $f_h(t)$, $f_{pto}(t)$, and $a(t)$ are the hydrodynamic force, PTO force, and heave acceleration of the oscillating body, respectively. The parameter m represents the total mass of the floater, the permanent magnet linear generator (PMLG) translator, and the interconnecting tether.

A. WAVE-FLOATER HYDRODYNAMIC MODEL

The hydrodynamic force is composed of the following forces:

$$f_h(t) = f_{ex}(t) + f_r(t) + f_b(t) + f_d(t), \quad (2)$$

where $f_{ex}(t)$, $f_r(t)$, $f_b(t)$, and $f_d(t)$ are the wave excitation, radiation, buoyancy, and drag forces, respectively. The wave excitation force is modeled in the time domain as the convolution of the excitation kernel function $k_{ex}(t)$ and the wave surface elevation $\xi(t)$,

$$f_{ex}(t) = k_{ex}(t) * \xi(t) = \int_0^t k_{ex}(\tau) \xi(t - \tau) d\tau. \quad (3)$$

The frequency-domain counterpart of (3) can be represented as

$$F_{ex}(i\omega) = K_{ex}(i\omega) \Xi(i\omega), \quad (4)$$

where $F_{ex}(i\omega)$ and $\Xi(i\omega)$ are the Fourier transform of the wave excitation force and wave elevation, respectively. The function $K_{ex}(i\omega)$ is the wave-to-excitation force FRF. The boundary element method (BEM) numerical tool

WAMIT is used to compute $K_{ex}(i\omega)$ for the range of wave frequencies under study. The numerical solution obtained from WAMIT is fitted to a proper transfer function, such as [2], [3]

$$F_{ex}(s) = K_{ex}(s) \Xi(s), \\ = \frac{b_m s^m + b_{m-1} s^{m-1} + \dots + b_0}{a_n s^n + a_{n-1} s^{n-1} + \dots + a_0} \Xi(s), \quad (5)$$

where $b_m, b_{m-1}, a_{n-1}, a_{n-2}, \dots, a_0, b_0$ represent the transfer function parameters, in which m and n are the order of the transfer function numerator and denominator, respectively. The variable s is the Laplace complex variable. Similarly, the radiation force is modeled as

$$f_r(t) = -m_\infty a(t) - \int_0^t k_r(\tau) v(t - \tau) d\tau. \quad (6)$$

Here, m_∞ and $k_r(t)$ are the added mass resulting from the water-floater interaction and the radiation kernel function, respectively. The radiation integral is approximated by

$$\int_0^t k_r(\tau) v(t - \tau) d\tau \approx C_r \gamma_r(t), \\ \dot{\gamma}_r(t) = A_r \gamma_r(t) + B_r v(t), \quad (7)$$

where $\gamma_r(t)$ is the radiation auxiliary state vector, and A_r , B_r , and C_r are the radiation force state matrices. The buoyancy force $f_b(t)$ is modeled as a function of heave displacement $z(t)$, where the buoyancy stiffness coefficient S_b is the constant of proportionality,

$$f_b(t) = -S_b z(t). \quad (8)$$

According to Morison’s equation, the viscous drag force $f_d(t)$ of a floating body is modeled as a quadratic function of the relative velocity between the floater and the water surface [13],

$$f_d(t) = -0.5\rho A_w C_d |v(t) - v_f(t)|(v(t) - v_f(t)), \quad (9)$$

where ρ , A_w , C_d , and $v_f(t)$ are sea water density, floater submerged surface area, viscous drag coefficient, and water surface heave velocity, respectively. Figure 2(a) depicts the viscous drag force as a function of the floater–wave relative velocity.

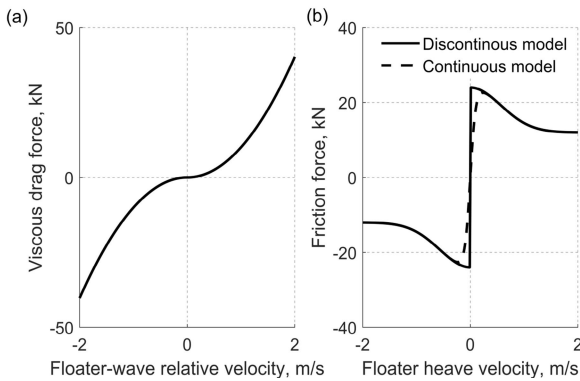


FIGURE 2. System nonlinear forces: (a) viscous drag force; (b) discontinuous and continuous PTO friction forces.

B. DIRECT-DRIVE PTO MODEL

The floater is tethered to a direct-drive PTO system placed on the sea floor. The PTO system consists of a surface-mounted PMLG and a restoring spring module, as shown in Fig. 1. The PMLG is responsible for converting the reciprocating heave motion of the floater to electrical power and simultaneously controlling the motion of the floater for optimum power absorption [14]. If one assumes that the permanent magnets are placed in the machine translator, which reciprocates linearly with respect to the stationary stator coils, the flux linkage $\psi_s(t)$ at the stator can be modeled as a function of the floater heave displacement $z(t)$,

$$\psi_s(t) = \psi_m \cos\left(\frac{\pi}{p_w} z(t)\right), \quad (10)$$

where ψ_m and p_w are the flux linkage amplitude and the machine pole pitch, respectively. According to Faraday’s law, the electromotive force (emf) $e(t)$ induced at the stator is given by

$$e(t) = -\frac{d\psi_s(t)}{dt}. \quad (11)$$

By substituting (10) in (11), the instantaneous three-phase emf voltages are derived as functions of $z(t)$ and $v(t)$ [14]:

$$e_a(t) = \frac{\pi \psi_m}{p_w} \sin\left(\frac{\pi}{p_w} z(t)\right) v(t), \quad (12)$$

$$e_b(t) = \frac{\pi \psi_m}{p_w} \sin\left(\frac{\pi}{p_w} z(t) - \frac{2\pi}{3}\right) v(t), \quad (13)$$

$$e_c(t) = \frac{\pi \psi_m}{p_w} \sin\left(\frac{\pi}{p_w} z(t) + \frac{2\pi}{3}\right) v(t). \quad (14)$$

The three-phase stator terminal voltage can be written in vector form as

$$v_{s,abc}(t) = e_{abc}(t) - Z_s(t) i_{s,abc}(t), \quad (15)$$

where $e_{abc}(t)$ is three-phase emf voltage vector, $i_{abc}(t)$ is the stator three-phase current vector, and $Z_s(t)$ is the PMLG stator synchronous impedance. The surface-mounted PMLG model in the synchronous reference frame is given by [15]

$$\frac{di_{sd}(t)}{dt} = -\frac{v_{sd}(t)}{L_s} - \frac{R_s}{L_s} i_{sd}(t) + \frac{\pi}{p_w} v(t) i_{sq}(t), \quad (16)$$

$$\frac{di_{sq}(t)}{dt} = -\frac{v_{sq}(t)}{L_s} - \frac{R_s}{L_s} i_{sq}(t) - \frac{\pi}{p_w} v(t) i_{sd}(t) - \frac{\pi \psi_{PM}}{p_w} v(t), \quad (17)$$

where $i_{sd}(t)$ and $i_{sq}(t)$ are the direct and quadrature components of the stator current, respectively. Similarly, $v_{sd}(t)$ and $v_{sq}(t)$ are the direct and quadrature components of the stator terminal voltage. The parameters R_s , L_s , and ψ_{PM} represent the stator resistance, inductance, and the fixed flux linkage resulting from the permanent magnets, respectively. The d – q components of the stator current and voltage are obtained using the Park–Clarke transformation [16], e.g.,

$$i_{s,dq}(t) = T(t)^T i_{s,abc}(t), \quad (18)$$

$$v_{s,dq}(t) = T(t)^T v_{s,abc}(t), \quad (19)$$

where

$$T(t) = \frac{2}{3} \begin{pmatrix} \cos\left(\frac{\pi}{p_w} z(t)\right) & -\sin\left(\frac{\pi}{p_w} z(t)\right) \\ \cos\left(\frac{\pi}{p_w} z(t) - \frac{2\pi}{3}\right) & -\sin\left(\frac{\pi}{p_w} z(t) - \frac{2\pi}{3}\right) \\ \cos\left(\frac{\pi}{p_w} z(t) + \frac{2\pi}{3}\right) & -\sin\left(\frac{\pi}{p_w} z(t) + \frac{2\pi}{3}\right) \end{pmatrix}. \quad (20)$$

The PMLG electromagnetic force $f_{em}(t)$ is evaluated as a function of the quadrature stator current as

$$f_{em}(t) = \frac{3\pi \psi_{PM}}{2p_w} i_{sq}(t). \quad (21)$$

By controlling the stator quadrature current $i_{sq}(t)$ using power converter modules, the electromagnetic force $f_{em}(t)$ can be manipulated, resulting in adjusting the motion of the floater to be in resonance with the wave excitation. Depending on the capabilities of the deployed power converter circuit and the sophistication of the associated control strategy, a near-optimum operation of the WEC can be achieved. As shown in Fig. 1, three types of loading scenarios are implemented in this study: three-phase resistive loading, three-phase diode rectifier loading, and three-phase boost rectifier loading. All three loading schemes produce electromagnetic force $f_{em}(t)$ with a damping effect; thus, $f_{em}(t)$ is in phase with the floater velocity $v(t)$ [14], [17]. The restoring spring force $f_{rs}(t)$, along with the gravitational force, supports the downward movement of the floater at wave troughs.

Also, it keeps the tether connecting the floater and the PMLG's translator well stretched, preventing unsynchronized movement between the two oscillating parts of the WEC [12]. The restoring force $f_{rs}(t)$ is modeled as a spring force with a restoring spring coefficient S_{rs} :

$$f_{rs}(t) = -S_{rs}z(t). \quad (22)$$

The friction force between the moving parts of the WEC can be modeled using the well-known Tustin model, which combines the Coulomb friction model with viscous and Stribeck effects [18], i.e.,

$$f_f(t) = -F_n\mu_d \operatorname{sgn}(v(t)) - \mu_v|v(t)| \operatorname{sgn}(v(t)) - F_n(\mu_s - \mu_d)e^{-\left(\frac{|v(t)|}{v_s}\right)^2} \operatorname{sgn}(v(t)), \quad (23)$$

where F_n , μ_d , μ_v , μ_s , and v_s are the normal force, the dynamic coefficient of friction, the viscous coefficient of friction, the static coefficient of friction, and the Stribeck velocity, respectively. The friction force model in (23) is nondifferentiable because of the discontinuity present in the Coulomb friction component (i.e., at $v(t) = 0$). Therefore, a continuous and differentiable approximation of the Tustin friction force model is needed. In [19], the following continuous velocity-dependent friction model is proposed:

$$f_f(t) \approx -F_n\mu_d \tanh(\alpha v(t)) - \mu_v v(t) - F_n(\mu_s - \mu_d)e^{-\left(\frac{|v(t)|}{v_s}\right)^2} \tanh(\alpha v(t)). \quad (24)$$

The tuning parameter α determines the rate of increase of the friction force from zero to the value of static friction. Dynamic models of the friction force described in (23) and (24) are shown in Fig. 2(b). The summation of the PMLG electromagnetic force $f_{em}(t)$, the restoring force $f_{rs}(t)$, and the friction force $f_f(t)$ make up the force contributed by the PTO system, $f_{pto}(t)$, depicted in (1).

C. WAVE-TO-WIRE WEC MODEL

The overall wave-to-wire nonlinear model of the system in continuous state space form can be expressed as

$$\dot{x}_1(t) = x_2(t), \quad (25)$$

$$\dot{x}_2(t) = \frac{1}{m + m_\infty} \left[f_{ex}(t) - \mathbf{C}_r \mathbf{x}_3(t) - (S_b + S_{rs})x_1(t) - 0.5\rho A_w C_d |x_2(t) - v_f(t)| (x_2(t) - v_f(t)) - \mu_v |x_2(t)| \operatorname{sgn}(x_2(t)) - F_n \mu_d \operatorname{sgn}(x_2(t)) - F_n(\mu_s - \mu_d)e^{-\left(\frac{|x_2(t)|}{v_s}\right)^2} \operatorname{sgn}(x_2(t)) + \frac{3\pi\psi_{PM}}{2p_w} x_5(t) \right], \quad (26)$$

$$\dot{\mathbf{x}}_3(t) = \mathbf{A}_r \mathbf{x}_3(t) + \mathbf{B}_r x_2(t), \quad (27)$$

$$\dot{x}_4(t) = -\frac{u_1(t)}{L_s} - \frac{R_s}{L_s} x_4(t) + \frac{\pi}{p_w} x_2(t) x_5(t), \quad (28)$$

$$\dot{x}_5(t) = -\frac{u_2(t)}{L_s} - \frac{R_s}{L_s} x_5(t) - \frac{\pi}{p_w} x_2(t) x_4(t) - \frac{\pi\psi_{PM}}{p_w} x_2(t), \quad (29)$$

$$\mathbf{y}(t) = \mathbf{x}(t), \quad (30)$$

where the state vector is $\mathbf{x}(t) = [x_1(t), x_2(t), \mathbf{x}_3(t), x_4(t), x_5(t)] = [z(t), v(t), \boldsymbol{\gamma}_r(t), i_{sd}(t), i_{sq}(t)]$, the system input vectors are $u_1(t) = v_{sd}(t)$ and $u_2(t) = v_{sq}(t)$, and the output vector is $\mathbf{y}(t) = [x_1(t), x_2(t), \mathbf{x}_3(t), x_4(t), x_5(t)]$. The wave radiation effect is modeled using the fourth-order linear model $\boldsymbol{\gamma}_r(t) \in \mathbb{R}^{4 \times 1}$. Therefore, the state and output vectors are $\mathbf{x}(t), \mathbf{y}(t) \in \mathbb{R}^{8 \times 1}$.

III. DERIVATION OF KALMAN-FILTER-BASED ESTIMATORS

In this section, three state estimators are derived: the proposed electrical-based extended Kalman filter (E-EKF) estimator, a mechanical-based extended Kalman filter (M-EKF) estimator, and a linearized version of the M-EKF estimator. All three estimators are designed to primarily estimate the floater's heave displacement, velocity, and wave excitation force.

A. DISCRETIZATION OF THE WEC MODEL

The system can be represented by the following generic discrete nonlinear model:

$$\mathbf{x}_k = \mathbf{f}_{k-1}(\mathbf{x}_{k-1}, \mathbf{u}_{k-1}, \mathbf{w}_{k-1}), \quad (31)$$

$$\mathbf{y}_k = \mathbf{g}_k(\mathbf{x}_k, \boldsymbol{\sigma}_k), \quad (32)$$

$$\mathbf{w}_k \sim (\mathbf{0}, \mathbf{Q}_k), \quad (33)$$

$$\boldsymbol{\sigma}_k \sim (\mathbf{0}, \mathbf{R}_k). \quad (34)$$

The functions \mathbf{f}_{k-1} and \mathbf{g}_k are nonlinear state and measurement functions at time instants $k-1$ and k , respectively. The state function estimates the system states at k using the state vector \mathbf{x}_{k-1} , the input vector \mathbf{u}_{k-1} , and the process noise vector \mathbf{w}_{k-1} evaluated at $k-1$. The process noise vector \mathbf{w}_k and the measurement noise vector $\boldsymbol{\sigma}_k$ are modeled as white noise with zero mean and known process noise and measurement noise covariance matrices of \mathbf{Q}_k and \mathbf{R}_k , respectively. Because the wave excitation force is meant to be estimated using other measured variables, the excitation force at k is modeled as a simple random walk process with drift [8], i.e.,

$$f_{ex,k} = f_{ex,k-1} + T_s \epsilon_{k-1}, \quad (35)$$

where T_s is the process sampling time and ϵ_{k-1} is the random walk drift at $k-1$, and it is modeled as a Gaussian noise process with zero mean. By updating the state equations in (25)–(30) to incorporate $f_{ex,k}$, the modified state vector evaluated at k is represented as $\mathbf{x}_k = [x_{1,k}, x_{2,k}, \mathbf{x}_{3,k}, x_{4,k}, x_{5,k}, x_{6,k}] = [z_k, v_k, \boldsymbol{\gamma}_{r,k}, f_{ex,k}, i_{sd,k}, i_{sq,k}] \in \mathbb{R}^{9 \times 1}$. The process noise vector $\mathbf{w}_k = [w_{1,k}, w_{2,k}, \mathbf{w}_{3,k}, w_{4,k}, w_{5,k}, w_{6,k}] \in \mathbb{R}^{9 \times 1}$. By using the backward Euler method, the set of differential equations in (25)–(30) are transformed to the following difference equations:

$$x_{1,k} = x_{1,k-1} + T_s x_{2,k-1} + T_s w_{1,k-1}, \quad (36)$$

$$x_{2,k} = x_{2,k-1} + \frac{T_s}{m + m_\infty} [x_{4,k-1} - \mathbf{C}_r \mathbf{x}_{3,k-1} - (S_b + S_{rs})x_{1,k-1}$$

$$- 0.5\rho A_w C_d (x_{2,k-1} - v_{f,k-1}) |x_{2,k-1} - v_{f,k-1}|$$

$$\begin{aligned}
 & -F_n \mu_d \tanh(\alpha x_{2,k-1}) \\
 & -F_n(\mu_s - \mu_d) e^{-\left(\frac{|x_{2,k-1}|}{v_s}\right)^2} \tanh(\alpha x_{2,k-1}) \\
 & -\mu_v x_{2,k-1} + \frac{3\pi \psi_{PM}}{2p_w} x_{6,k-1} \Big] + T_s w_{2,k-1}, \quad (37)
 \end{aligned}$$

$$\begin{aligned}
 \mathbf{x}_{3,k} &= \mathbf{x}_{3,k-1} + T_s [\mathbf{A}_r \mathbf{x}_{3,k-1} + \mathbf{B}_r x_{2,k-1}] \\
 & + T_s w_{3,k-1}, \quad (38)
 \end{aligned}$$

$$x_{4,k} = x_{4,k-1} + T_s w_{4,k-1}, \quad (39)$$

$$\begin{aligned}
 x_{5,k} &= x_{5,k-1} + \frac{T_s}{L_s} [-u_{1,k-1} - R_s x_{5,k-1} \\
 & + \frac{\pi L_s}{p_w} x_{2,k-1} x_{6,k-1}] + T_s w_{5,k-1}, \quad (40)
 \end{aligned}$$

$$\begin{aligned}
 x_{6,k} &= x_{6,k-1} + \frac{T_s}{L_s} [-u_{2,k-1} - R_s x_{6,k-1} \\
 & - \frac{\pi L_s}{p_w} x_{2,k-1} x_{5,k-1} - \frac{\pi \psi_{PM}}{p_w} x_{2,k-1}] + T_s w_{6,k-1}, \quad (41)
 \end{aligned}$$

$$y_{1,k} = x_{5,k} + \sigma_{1,k}, \quad (42)$$

$$y_{2,k} = x_{6,k} + \sigma_{2,k}. \quad (43)$$

The excitation force random walk drift ϵ_{k-1} in (35) is

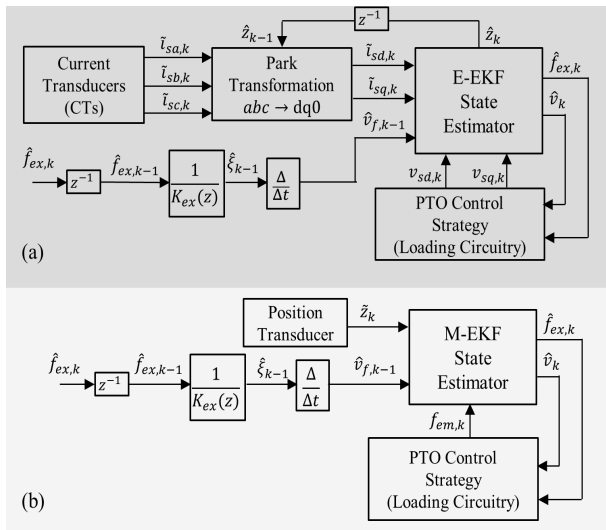


FIGURE 3. State estimator block diagrams: (a) E-EKF estimator; (b) M-EKF estimator.

replaced with the system noise variable $w_{4,k-1}$ in (39). Moreover, the discretized version of the continuous friction model depicted in (24) is used instead of (23).

B. PROPOSED E-EKF ESTIMATOR

The nonlinear system model described in (36)–(43) is utilized to derive the E-EKF estimator. The E-EKF estimator is fed with the measured three-phase stator currents (using CTs) after transforming them to their d - q counterparts ($\tilde{i}_{sd,k}$ and $\tilde{i}_{sq,k}$) using (18) and the stator voltages in the d - q reference

frame ($v_{sd,k}$ and $v_{sq,k}$) computed by the adopted PTO control strategy, as shown in Fig. 3(a). The Jacobian matrix of the state function \mathbf{f}_{k-1} is computed with respect to the state vector \mathbf{x}_{k-1} as follows:

$$\begin{aligned}
 \mathbf{F}_{k-1} &= \frac{\partial \mathbf{f}_{k-1}}{\partial \mathbf{x}_{k-1}} \\
 &= \begin{pmatrix} \frac{\partial f_{1,k-1}}{\partial x_{1,k-1}} & \frac{\partial f_{1,k-1}}{\partial x_{2,k-1}} & \frac{\partial f_{1,k-1}}{\partial x_{3,k-1}} & \cdots & \frac{\partial f_{1,k-1}}{\partial x_{6,k-1}} \\ \frac{\partial f_{2,k-1}}{\partial x_{1,k-1}} & \frac{\partial f_{2,k-1}}{\partial x_{2,k-1}} & \cdots & \cdots & \frac{\partial f_{2,k-1}}{\partial x_{6,k-1}} \\ \frac{\partial f_{3,k-1}}{\partial x_{1,k-1}} & \cdots & \cdots & \cdots & \vdots \\ \vdots & \cdots & \cdots & \cdots & \vdots \\ \frac{\partial f_{6,k-1}}{\partial x_{1,k-1}} & \frac{\partial f_{6,k-1}}{\partial x_{2,k-1}} & \frac{\partial f_{6,k-1}}{\partial x_{3,k-1}} & \cdots & \frac{\partial f_{6,k-1}}{\partial x_{6,k-1}} \end{pmatrix}, \quad (44)
 \end{aligned}$$

where the Jacobian matrix $\mathbf{F}_{k-1} \in \mathbb{R}^{9 \times 9}$ entries are evaluated as follows:

$$\begin{aligned}
 \frac{\partial f_{1,k-1}}{\partial x_{1,k-1}} &= 1, \quad \frac{\partial f_{1,k-1}}{\partial x_{2,k-1}} = T_s, \quad \frac{\partial f_{1,k-1}}{\partial x_{3,k-1}} = \mathbf{0}_{1 \times 4}, \quad \frac{\partial f_{1,k-1}}{\partial x_{4,k-1}} = 0, \\
 \frac{\partial f_{1,k-1}}{\partial x_{5,k-1}} &= \frac{\partial f_{1,k-1}}{\partial x_{6,k-1}} = 0, \quad \frac{\partial f_{2,k-1}}{\partial x_{1,k-1}} = \frac{T_s(S_b + S_{rs})}{m + m_\infty}, \\
 \frac{\partial f_{2,k-1}}{\partial x_{2,k-1}} &= 1 + \frac{T_s}{m + m_\infty} [-\rho A_w C_d (x_{2,k-1} - v_{f,k-1}) \\
 & - \alpha F_n \mu_d \operatorname{sech}^2(\alpha x_{2,k-1}) - \mu_v \\
 & - F_n(\mu_s - \mu_d) \alpha e^{-\left(\frac{|x_{2,k-1}|}{v_s}\right)^2} \operatorname{sech}^2(\alpha x_{2,k-1}) \\
 & - \frac{2F_n(\mu_s - \mu_d)x_{2,k-1}}{v_s^2} \\
 & \times e^{-\left(\frac{|x_{2,k-1}|}{v_s}\right)^2} \tanh(\alpha x_{2,k-1})], \\
 \frac{\partial f_{2,k-1}}{\partial x_{3,k-1}} &= \frac{-T_s C_r}{m + m_\infty}, \quad \frac{\partial f_{2,k-1}}{\partial x_{4,k-1}} = \frac{T_s}{m + m_\infty}, \quad \frac{\partial f_{2,k-1}}{\partial x_{5,k-1}} = 0, \\
 \frac{\partial f_{2,k-1}}{\partial x_{6,k-1}} &= \frac{3\pi \psi_{PM} T_s}{2p_w(m + m_\infty)}, \quad \frac{\partial f_{3,k-1}}{\partial x_{1,k-1}} = \mathbf{0}_{4 \times 1}, \\
 \frac{\partial f_{3,k-1}}{\partial x_{2,k-1}} &= T_s \mathbf{B}_r, \quad \frac{\partial f_{3,k-1}}{\partial x_{3,k-1}} = \mathbf{I} + T_s \mathbf{A}_r, \quad \frac{\partial f_{3,k-1}}{\partial x_{4,k-1}} = \mathbf{0}_{4 \times 1}, \\
 \frac{\partial f_{3,k-1}}{\partial x_{5,k-1}} &= \frac{\partial f_{3,k-1}}{\partial x_{6,k-1}} = \mathbf{0}_{4 \times 1}, \\
 \frac{\partial f_{4,k-1}}{\partial x_{1,k-1}} &= \frac{\partial f_{4,k-1}}{\partial x_{2,k-1}} = 0, \quad \frac{\partial f_{4,k-1}}{\partial x_{3,k-1}} = \mathbf{0}_{1 \times 4}, \quad \frac{\partial f_{4,k-1}}{\partial x_{4,k-1}} = 1, \\
 \frac{\partial f_{4,k-1}}{\partial x_{5,k-1}} &= \frac{\partial f_{4,k-1}}{\partial x_{6,k-1}} = 0, \quad \frac{\partial f_{5,k-1}}{\partial x_{1,k-1}} = 0, \quad \frac{\partial f_{5,k-1}}{\partial x_{2,k-1}} \\
 &= \frac{\pi T_s}{p_w} x_{6,k-1}, \\
 \frac{\partial f_{5,k-1}}{\partial x_{3,k-1}} &= \mathbf{0}_{1 \times 4}, \quad \frac{\partial f_{5,k-1}}{\partial x_{4,k-1}} = 0, \quad \frac{\partial f_{5,k-1}}{\partial x_{5,k-1}} = 1 - \frac{R_s T_s}{L_s},
 \end{aligned}$$

$$\begin{aligned}\frac{\partial f_{5,k-1}}{\partial x_{6,k-1}} &= \frac{\pi T_s}{\rho w} x_{2,k-1}, \quad \frac{\partial f_{6,k-1}}{\partial x_{1,k-1}} = 0, \\ \frac{\partial f_{6,k-1}}{\partial x_{2,k-1}} &= -\frac{\pi T_s}{\rho w} x_{5,k-1} - \frac{\pi \psi_{PM} T_s}{\rho w L_s}, \quad \frac{\partial f_{6,k-1}}{\partial x_{3,k-1}} = \mathbf{0}_{1 \times 4}, \\ \frac{\partial f_{6,k-1}}{\partial x_{4,k-1}} &= 0, \quad \frac{\partial f_{6,k-1}}{\partial x_{5,k-1}} = -\frac{\pi T_s}{\rho w} x_{2,k-1}, \\ \frac{\partial f_{6,k-1}}{\partial x_{6,k-1}} &= 1 - \frac{R_s T_s}{L_s}.\end{aligned}$$

The state Jacobian matrix $\mathbf{F}_{k-1} \in \mathbb{R}^{9 \times 9}$ is evaluated at the posteriori state vector $\hat{\mathbf{x}}_{k-1}^+$. The posteriori state vector $\hat{\mathbf{x}}_{k-1}^+$ and the posteriori estimation error covariance matrix \mathbf{P}_{k-1}^+ are initiated as $\hat{\mathbf{x}}_0^+ = \mathbf{0}_{9 \times 1}$ and $\mathbf{P}_0^+ = \mathbf{0}_{9 \times 9}$, respectively. The time update (prediction) equations of the E-EKF estimator are given by [20]

$$\mathbf{P}_k^- = \mathbf{F}_{k-1} \mathbf{P}_{k-1}^+ \mathbf{F}_{k-1}^\top + \mathbf{W}_{k-1} \mathbf{Q}_{e,k-1} \mathbf{W}_{k-1}^\top, \quad (45)$$

$$\hat{\mathbf{x}}_k^- = \mathbf{f}_{k-1}(\hat{\mathbf{x}}_{k-1}^+, u_{k-1}, \mathbf{0}), \quad (46)$$

where \mathbf{P}_k^- is the priori estimation error covariance matrix and $\hat{\mathbf{x}}_k^-$ is the priori estimated state vector. The process noise Jacobian matrix \mathbf{W}_{k-1} is computed as

$$\mathbf{W}_{k-1} = \frac{\partial \mathbf{f}_{k-1}}{\partial \mathbf{w}_{k-1}} = T_s \mathbf{I}_{9 \times 9} \in \mathbb{R}^{9 \times 9}. \quad (47)$$

The square matrix $\mathbf{I}_{9 \times 9}$ is an identity matrix and $\mathbf{Q}_{e,k-1} \in \mathbb{R}^{9 \times 9}$ is the process noise covariance matrix. The measurement update (correction) equations are

$$\mathbf{K}_k = \mathbf{P}_k^- \mathbf{H}_k^\top (\mathbf{H}_k \mathbf{P}_k^- \mathbf{H}_k^\top + \mathbf{D}_k \mathbf{R}_{e,k} \mathbf{D}_k^\top)^{-1}, \quad (48)$$

$$\hat{\mathbf{x}}_k^+ = \hat{\mathbf{x}}_k^- + \mathbf{K}_k [\mathbf{y}_k - \mathbf{g}_k(\hat{\mathbf{x}}_k^-, \mathbf{0})], \quad (49)$$

$$\mathbf{P}_k^+ = (\mathbf{I} - \mathbf{K}_k \mathbf{H}_k) \mathbf{P}_k^-, \quad (50)$$

where \mathbf{K}_k and $\mathbf{R}_{e,k} \in \mathbb{R}^{9 \times 9}$ are the Kalman filter gain and the measurement noise covariance matrices at time instant k , respectively. The measurement equation Jacobian matrices \mathbf{H}_k and \mathbf{D}_k are defined as

$$\mathbf{H}_k = \frac{\partial \mathbf{g}_k}{\partial \mathbf{x}_k} = \begin{pmatrix} 0 & 0 & \mathbf{0}_{1 \times 4} & 0 & 1 & 0 \\ 0 & 0 & \mathbf{0}_{1 \times 4} & 0 & 0 & 1 \end{pmatrix} \in \mathbb{R}^{2 \times 9}, \quad (51)$$

$$\mathbf{D}_k = \frac{\partial \mathbf{g}_k}{\partial \boldsymbol{\sigma}_k} = \begin{pmatrix} 0 & 0 & \mathbf{0}_{1 \times 4} & 0 & 1 & 0 \\ 0 & 0 & \mathbf{0}_{1 \times 4} & 0 & 0 & 1 \end{pmatrix} \in \mathbb{R}^{2 \times 9}. \quad (52)$$

The E-EKF estimator requires real-time information about the water surface velocity to evaluate the viscous drag force in (26). Therefore, a one-sample delayed estimate of the excitation force $\hat{f}_{ex,k-1}$ is fed back and the wave elevation $\hat{\xi}_{k-1}$ is estimated using the reciprocal of the wave-to-force transfer function $1/\mathbf{K}_{ex}(s)$ described in (5). By differentiating $\hat{\xi}_{k-1}$, the water surface velocity $\hat{v}_{f,k-1}$ is estimated, as shown in Fig. 3(a). Despite the modeling inaccuracies associated with $\mathbf{K}_{ex}(s)$, this approach is a low-cost alternative to installing equipment specifically dedicated to measure ξ_k and/or $v_{f,k}$ in real time. Furthermore, the drag force $f_{d,k}$ is significantly smaller in magnitude than other dominating hydrodynamic forces (e.g., $f_{ex,k}$ and $f_{b,k}$); therefore, a trade-off between modeling fidelity and cost is tolerable. Similarly, the measured three-phase stator currents are transformed to

their d - q counterparts via feeding back the estimated heave displacement \hat{z}_{k-1} to be used by the Park–Clarke transform.

C. M-EKF ESTIMATOR

The M-EKF estimator receives measured heave displacement readings using a linear position transducer and the computed PMLG electromagnetic force $f_{em}(t)$, as depicted in Fig. 3(b). The state equations in (36)–(43) are modified to be only confined to the system’s mechanical dynamics through omitting the PMLG state equations described in (40) and (41). As a result, the state equation in (37) is adjusted accordingly to include the PMLG electromechanical force $f_{em,k}$ denoted as the system input u_k :

$$x_{1,k} = x_{1,k-1} + T_s x_{2,k-1} + T_s w_{1,k-1}, \quad (53)$$

$$\begin{aligned}x_{2,k} &= x_{2,k-1} + \frac{T_s}{m + m_\infty} [x_{4,k-1} - \mathbf{C}_r \mathbf{x}_{3,k-1} \\ &\quad - (S_b + S_{rs}) x_{1,k-1} \\ &\quad - 0.5 \rho A_w C_d (x_{2,k-1} - v_{f,k-1}) |x_{2,k-1} - v_{f,k-1}| \\ &\quad - F_n \mu_d \tanh(\alpha x_{2,k-1}) \\ &\quad - F_n (\mu_s - \mu_d) e^{-\left(\frac{|x_{2,k-1}|}{v_s}\right)^2} \tanh(\alpha x_{2,k-1}) \\ &\quad - \mu_v x_{2,k-1} + u_{k-1}] + T_s w_{2,k-1},\end{aligned} \quad (54)$$

$$\begin{aligned}x_{3,k} &= \mathbf{x}_{3,k-1} + T_s [\mathbf{A}_r \mathbf{x}_{3,k-1} + \mathbf{B}_r x_{2,k-1}] \\ &\quad + T_s \mathbf{w}_{3,k-1},\end{aligned} \quad (55)$$

$$x_{4,k} = x_{4,k-1} + T_s w_{4,k-1}, \quad (56)$$

$$y_k = x_{1,k} + \sigma_{1,k}. \quad (57)$$

The corresponding Jacobian matrix for the M-EKF estimator is

$$\begin{aligned}\mathbf{F}_{k-1} &= \frac{\partial \mathbf{f}_{k-1}}{\partial \mathbf{x}_{k-1}} \\ &= \begin{pmatrix} \frac{\partial f_{1,k-1}}{\partial x_{1,k-1}} & \frac{\partial f_{1,k-1}}{\partial x_{2,k-1}} & \frac{\partial f_{1,k-1}}{\partial \mathbf{x}_{3,k-1}} & \frac{\partial f_{1,k-1}}{\partial x_{4,k-1}} \\ \frac{\partial f_{2,k-1}}{\partial x_{1,k-1}} & \frac{\partial f_{2,k-1}}{\partial x_{2,k-1}} & \frac{\partial f_{2,k-1}}{\partial \mathbf{x}_{3,k-1}} & \frac{\partial f_{2,k-1}}{\partial x_{4,k-1}} \\ \frac{\partial \mathbf{f}_{3,k-1}}{\partial x_{1,k-1}} & \frac{\partial \mathbf{f}_{3,k-1}}{\partial x_{2,k-1}} & \frac{\partial \mathbf{f}_{3,k-1}}{\partial \mathbf{x}_{3,k-1}} & \frac{\partial \mathbf{f}_{3,k-1}}{\partial x_{4,k-1}} \\ \frac{\partial f_{4,k-1}}{\partial x_{1,k-1}} & \frac{\partial f_{4,k-1}}{\partial x_{2,k-1}} & \frac{\partial f_{4,k-1}}{\partial \mathbf{x}_{3,k-1}} & \frac{\partial f_{4,k-1}}{\partial x_{4,k-1}} \end{pmatrix}.\end{aligned} \quad (58)$$

Similar to the E-EKF estimator derived in Section III-B, the estimated state vector and the estimation error covariance matrix are initiated as $\hat{\mathbf{x}}_0^+ = \mathbf{0}_{7 \times 1}$ and $\mathbf{P}_0^+ = \mathbf{0}_{7 \times 7}$. The M-EKF estimator covariance matrices $\mathbf{Q}_{m,k-1} \in \mathbb{R}^{7 \times 7}$ and $\mathbf{R}_{m,k} \in \mathbb{R}^{7 \times 7}$ are adequately tailored. The estimator’s measurement Jacobian matrices are

$$\mathbf{H}_k = \mathbf{D}_k = (1 \ 0 \ \mathbf{0}_{1 \times 4} \ 0) \in \mathbb{R}^{1 \times 7}. \quad (59)$$

D. LINEAR KALMAN FILTER ESTIMATOR

The linear Kalman filter (KF) estimator shares the same input signals as the M-EKF. It is derived by linearizing the system state-space model in (53)–(57). By omitting the drag force and friction force dynamics, the resultant linear time-invariant (LTI) model is

$$x_k = A_l x_{k-1} + B_l u_{k-1} + w_{k-1}, \tag{60}$$

$$y_k = C_l I_k + \sigma_k, \tag{61}$$

where

$$A_l = \begin{pmatrix} A_d & B_d \\ \mathbf{0}_{1 \times 6} & 1 \end{pmatrix}, B_l = \begin{pmatrix} B_d \\ 0 \end{pmatrix}, C_l = (C_d \ 0).$$

The state matrices A_d , B_d , and C_d are the discrete versions of the following continuous state matrices:

$$A = \begin{pmatrix} 0 & 1 & \mathbf{0}_{1 \times 4} \\ -\frac{S_b + S_{rs}}{m + m_\infty} & 0 & -\frac{C_r}{m + m_\infty} \\ \mathbf{0}_{4 \times 1} & B_r & A_r \end{pmatrix} \in \mathbb{R}^{6 \times 6},$$

$$B = \begin{pmatrix} 0 \\ \frac{1}{m + m_\infty} \\ \mathbf{0}_{4 \times 1} \end{pmatrix} \in \mathbb{R}^{6 \times 1}, C = (1 \ 0 \ 0 \ 0 \ 0 \ 0) \in \mathbb{R}^{1 \times 6}.$$

By initializing the posteriori estimate of the state vector as $\hat{x}_o^+ = \mathbf{0}_{7 \times 1}$ and the posteriori estimation error covariance matrix as $P_o^+ = \mathbf{0}_{7 \times 7}$, the state estimate (\hat{x}_k^+) is computed at every sampling instant using the following equations [20]:

$$P_k^- = A_l P_{k-1}^+ A_l^\top + Q_{ml,k-1}, \tag{62}$$

$$K_k = P_k^- C_l^\top (C_l P_k^- C_l^\top + R_{ml,k})^{-1}, \tag{63}$$

$$\hat{x}_k^- = A_l \hat{x}_{k-1}^+ + B_l u_{k-1}, \tag{64}$$

$$\hat{x}_k^+ = \hat{x}_k^- + K_k (y_k - C_l \hat{x}_k^-), \tag{65}$$

$$P_k^+ = (I - K_k C_l) P_k^-, \tag{66}$$

where P_k^- , P_k^+ , and K_k are the priori error covariance matrix at k , posteriori error covariance matrix at k , and the KF gain at k , respectively. The matrices $Q_{ml,k-1} \in \mathbb{R}^{7 \times 7}$ and $R_{ml,k} \in \mathbb{R}^{7 \times 7}$ are the process and measurement noise covariance matrices of the linearized KF, respectively.

IV. RESULTS AND DISCUSSION

A. SIMULATION SETUP AND PERFORMANCE METRICS

The performance of the developed state estimators is analyzed through simulations performed in Simulink/MATLAB. A point absorber WEC with a single-body cylindrical floater is implemented. The design parameters of the investigated WEC system are listed in Appendix A.

Different performance metrics are deployed to assess the goodness of the developed state estimators. The first is the normalized mean square error (NMSE), which measures the discrepancy between the true and estimated states. Here, the true excitation force $f_{ex,k}$ is the one actually experienced by the floater in the WEC plant, and it is computed using the model described in (5), whereas the floater’s true velocity is computed using the WEC wave-to-wire model

depicted in (25)–(30). The root mean squared error (RMSE) is also used to measure the estimator accuracy along with the estimation error deviation from zero. To check whether the developed estimators produce unbiased estimates, estimation bias (EB) is deployed. A new metric is proposed in this study: the excitation energy percentage error (EEPE). This metric is introduced to assess how much wave excitation energy is lost as a result of the estimation technique compared to the true available excitation energy. The EEPE is calculated as

$$EEPE(\%) = \frac{E_{ex} - \hat{E}_{ex}}{E_{ex}} \times 100, \tag{67}$$

where E_{ex} and \hat{E}_{ex} are the true and estimated excitation energies, respectively. The true excitation energy is computed as $E_{ex} = T_s \sum_{k=1}^m f_{ex,k} v_k$, whereas the estimated incident energy is $\hat{E}_{ex} = T_s \sum_{k=1}^m \hat{f}_{ex,k} \hat{v}_k$. The EEPE metric gives a compound measure of the estimation accuracy for both the excitation force and the floater’s heave velocity. The upper limit of the summation m is the simulation run time duration.

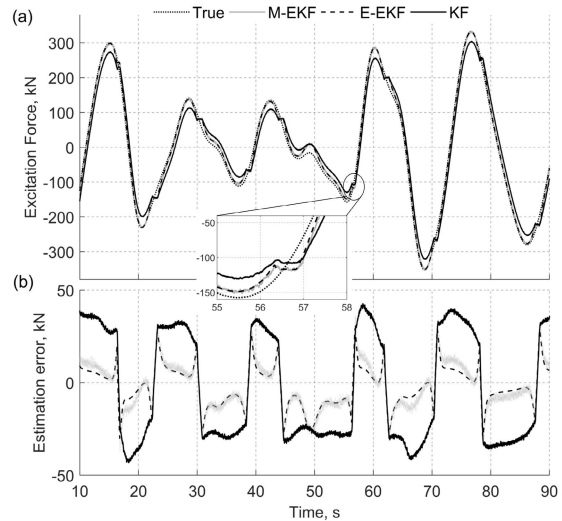


FIGURE 4. Performance of the E-EKF, M-EKF, and KF estimators under an irregular sea state of $H_s = 3.5$ m and $T_p = 15$ s and a linear (resistive) load: (a) excitation force estimates; (b) estimation error.

B. EFFECT OF SEA ENVIRONMENT CHARACTERISTICS

The developed estimators are tested under various irregular sea states with different significant heights H_s and peak periods T_p . The irregular sea states are generated using the JONSWAP spectrum. Initially, the PMLG is connected to a three-phase resistive load (linear load) with per phase resistance of $R_l = 5 \Omega$. An irregular sea state of $H_s = 3.5$ m and $T_p = 15$ s is applied and the state estimator performances are examined. As shown in Fig. 4, all three estimators managed to estimate the wave excitation force adequately, although the linearized KF estimator produced a higher (by almost a factor of 2) estimation error, as shown in Fig. 4(b). The enlarged portion of Fig. 4(a) showcases the performance of the estimators at the instant when the friction force reaches

TABLE 1. Applied irregular sea states (SS) generated using the JONSWAP spectrum.

Parameter (unit)	SS1	SS2	SS3	SS4	SS5	SS6	SS7	SS8
Significant height H_s (m)	2	2.2	3	2.6	2.6	1.75	2.5	3.5
Peak period T_p (s)	8	9	10	11	12	13	14	15
Wave power level J_w (kW/m)	15.11	20.62	43.02	36.22	39.21	18.66	41.26	89.34

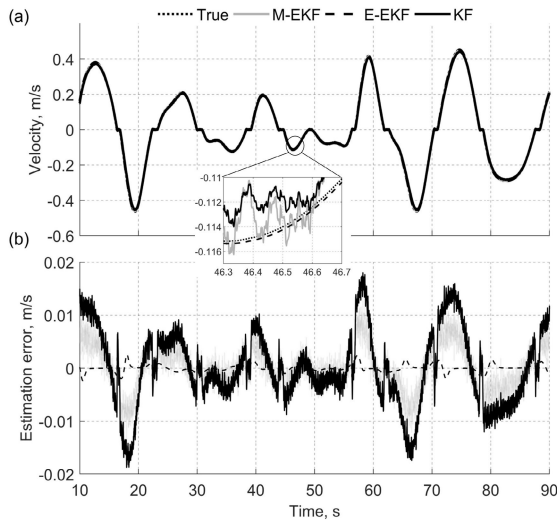


FIGURE 5. Performance of the E-EKF, M-EKF, and KF estimators under an irregular sea state of $H_s = 3.5$ m and $T_p = 15$ s and a linear (resistive) load: (a) heave velocity estimates; (b) estimation error.

its maximum value – in the vicinity of zero floater velocity ($v(t) \approx 0$ m/s). The E-EKF estimator outperformed the other two estimators in terms of the excitation force estimation accuracy, producing an NMSE value of 0.95 compared to 0.92 and 0.83 for the M-EKF and linearized KF, respectively. In terms of velocity, all three estimators produced accurate estimates (as shown in Fig. 5) with a slight advantage for the E-EKF estimator with an NMSE score of 0.99, compared to scores of 0.98 and 0.96 for the M-EKF and KF estimators, respectively. As depicted in Fig. 5(b), the E-EKF estimator generated a significantly less noisy estimate (dashed line) compared to the other estimators. As a result of its superior performance in estimating the wave excitation force and floater’s heave velocity, the E-EKF estimator produced a low EEPE score of 3.85%, whereas the M-EKF and KF estimators scored 6.28% and 31.08%, respectively.

To further analyze the developed estimators, various polychromatic sea states with varying significant height H_s and peak period T_p values are applied. Table 1 summarizes the characteristics of the deployed sea states. In Fig. 6, the performance of the three estimators in estimating the wave excitation force is compared using four different performance metrics, namely, NMSE, EB, RMSE, and EEPE. The E-EKF

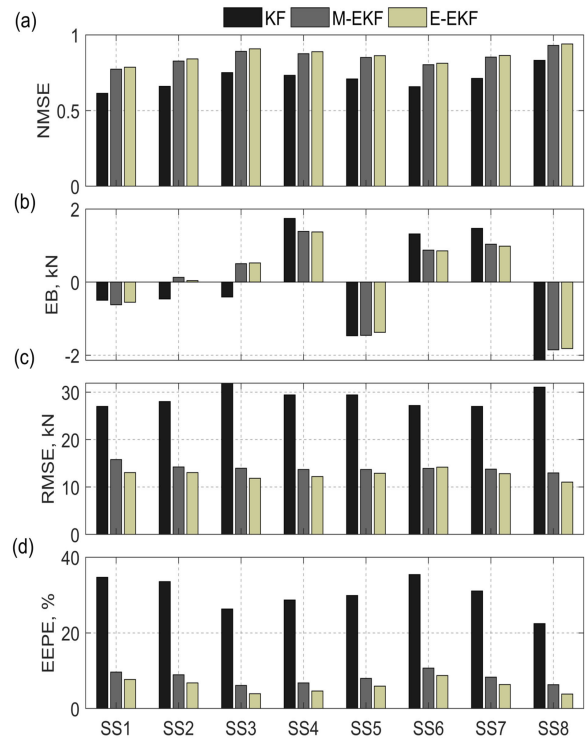


FIGURE 6. State estimator performance in estimating the wave excitation force under various sea-state conditions.

estimator outperformed the other two estimators with a minimum NMSE score of 0.79 and a maximum score of 0.95, as shown in Fig. 6(a). The estimation error of the proposed E-EKF characterized by the NMSE is influenced by the sea-state power level J_w , where the estimator scores higher NMSE for energetic sea states (e.g., SS3, SS7, and SS8). All three estimators proved to be unbiased, as shown in Fig. 6(b). Both E-EKF and M-EKF estimators managed to generate estimates with relatively low estimation error variance (i.e., $RMSE < 15$ kN) compared to the linearized KF estimator (i.e., $RMSE > 25$ kN), as depicted in Fig. 6(c). Moreover, the RMSE scores show that the E-EKF and M-EKF estimators are independent of the sea-state characteristics. As shown in Fig. 6(d), the E-EKF estimator exhibited superior performance in terms of the EEPE metric with a minimum score of 3.85% and maximum score of 8.73%. Lower EEPE values are attributed not only to higher NMSE scores for the wave excitation force estimates but also to higher

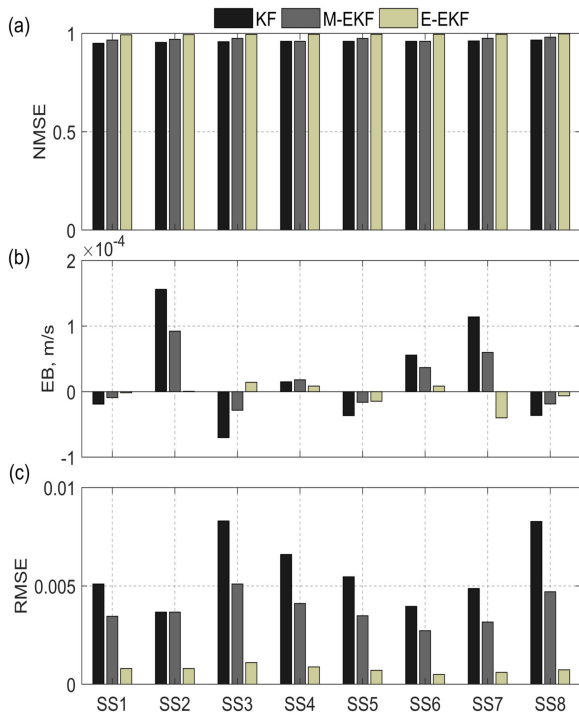


FIGURE 7. State estimator performance in estimating the WEC heave velocity under various sea-state conditions.

NMSE scores (i.e., $NMSE > 0.99$) for the floater velocity estimates, as shown in Fig. 7(a). Furthermore, the E-EKF estimator proved to be less prone to measurement noise. This is particularly evident in its RMSE scores (i.e., $RMSE < 1 \times 10^{-3}$ m/s) compared to the other two estimators shown in Fig. 7(c).

C. SENSITIVITY TO MODELING MISMATCHES

Modeling inaccuracies and mismatches are a common problem in complex nonlinear systems – and WECs are no different. The proposed state estimator is further tested against linear and nonlinear perturbations in a system plant model in (25)–(30). The viscous drag force is perturbed linearly by varying the drag coefficient C_d by $\pm 15\%$ from its nominal value $C_d = 1$, as shown in Fig. 8(a). The friction dynamics are set to zero in both the plant and estimator models. A relatively slow sea state of $H_s = 2.2$ m and $T_p = 14$ s is applied and the performance of the three developed estimators is examined using EEPE as a metric. The E-EKF estimator outperformed the other two estimators with EEPE $\leq 2\%$, as shown in Fig. 8(b). However, the rate of change of EEPE over the perturbation range for the E-EKF estimator is greater than that of both the M-EKF and KF estimators. Hence, the E-EKF estimator is more sensitive to the linear perturbation in the drag force, which is beneficial when C_d decreases. The opposite is true for higher frequency sea states (i.e., $H_s = 2.2$ m and $T_s = 9$ s), in which the E-EKF estimator is less sensitive to linear variations in the drag force, as shown in Fig. 8(c). Similarly, the friction force is

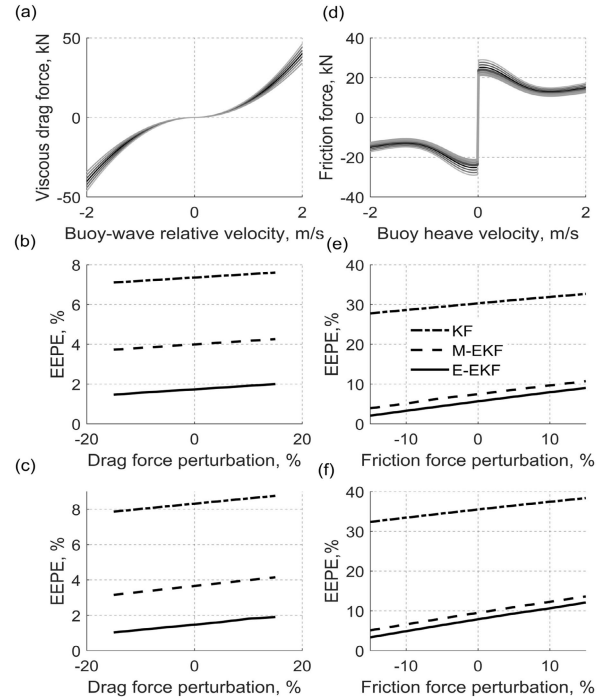


FIGURE 8. E-EKF, M-EKF and KF estimator performances under linear perturbations: (a) $\pm 15\%$ perturbations in $f_d(t)$; (b) EEPE score for a slow sea state under perturbations in $f_d(t)$; (c) EEPE score for a fast sea state under perturbations in $f_d(t)$; (d) $\pm 15\%$ perturbations in $f_f(t)$; (e) EEPE score for a slow sea state under perturbations in $f_f(t)$; (f) EEPE score for a fast sea state under perturbations in $f_f(t)$.

perturbed linearly by $\pm 15\%$ while keeping a nominal drag force setting and the estimator performances were compared, as depicted in Fig. 8(d). By applying both slow and fast traveling sea states, the E-EKF estimator exhibited more sensitivity to variations in the friction force compared to the other estimators, although scoring lower EEPE values, as shown in Figs. 8(e) and 8(f).

Subsequently, nonlinear perturbations were applied on the plant’s friction force model, particularly, the friction Stribeck effect component. As shown in Fig. 9(a), by varying the Stribeck velocity v_s , the level of nonlinearity at low velocity values can be varied. For an irregular sea state of $H_s = 2.2$ m and $T_p = 14$ s, all three estimators maintained almost a fixed EEPE value for $v_s > 1$ m/s, where the E-EKF estimator produced superior performance compared to the M-EKF estimator, as shown in Fig. 9(b). The value of EEPE of the E-EKF and M-EKF estimators gradually drops for $v_s < 1$ m/s. For the more rapid sea state ($H_s = 2.2$ m and $T_s = 9$ s), the E-EKF and M-EKF estimators are less sensitive to changes in v_s . Nevertheless, both estimators suffer from a sharp drop in EEPE for $v_s < 0.5$ m/s (Fig. 9(c)).

D. SENSITIVITY TO MEASUREMENT NOISE

Having concise knowledge of the characteristics of the noise associated with measured quantities that describe the current state of the physical phenomena is one of the most important

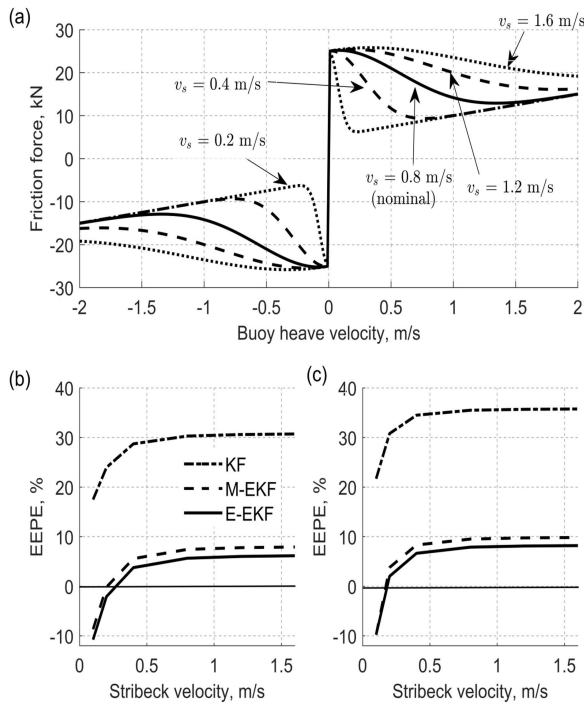


FIGURE 9. E-EKF, M-EKF and KF estimator performances in estimating $f_{ex,k}$ under nonlinear parametric perturbations in the friction force Stribeck velocity v_s .

aspects of designing state estimators. Unlike process noise, measurement noise is usually readily characterized in the information provided by sensor and transducer manufacturers. Precise characterization of the noise that might contaminate the measured signals facilitates the process of tuning the noise covariance matrix R_k . Despite adequate pre-deployment tuning of R_k , measurement noise could be induced by external factors such as vibration and electromagnetic interference. Here, the E-EKF estimator is fed with three-phase stator current measurements $i_{s,abc}(t)$ using CTs, as shown in Fig. 3(a). Nominally, the CT measurement noise is modeled as white noise with zero mean and a variance of 1×10^{-4} A, indicating low noise contamination. This is demonstrated in Fig. 10(a), where the measured phase stator current is plotted with and without measurement noise. White noise of zero mean and 1 A variance is applied to the three-phase stator current measurements and the corresponding effect on the E-EKF estimator performance is examined. As shown in Fig. 10(b), both noisy and unnoisy current measurements resulted in the same EEPE score of approximately 9%. Logarithmically varying the measurement noise variance of the stator currents has no effect on the excitation force estimation, as it produced a fixed RMSE value (i.e., RMSE = 11.7 kN), as demonstrated in Fig. 10(c). This behavior of the proposed E-EKF estimator is based on the nature of the abc to dq transformation or Park–Clarke transformation depicted in (20), which not only transforms the three-phase synchronous current signals to a couple of low-frequency signals but also acts like a low-pass filter

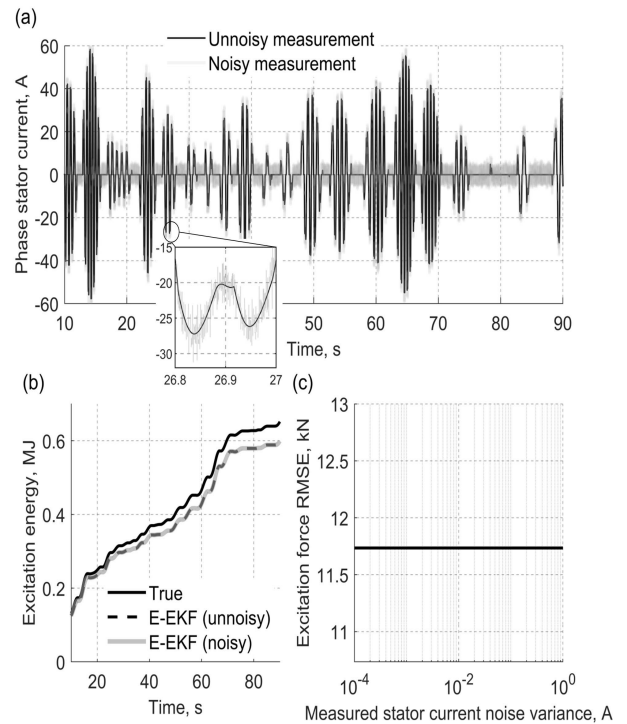


FIGURE 10. E-EKF estimator performance under varying CT measurement noise variance: (a) Noisy and unnoisy stator phase current; (b) accumulated excitation energy for true E-EKF estimate (noisy) and E-EKF estimate (unnoisy); (c) RMSE of the E-EKF wave excitation estimates under varying current measurement noise.

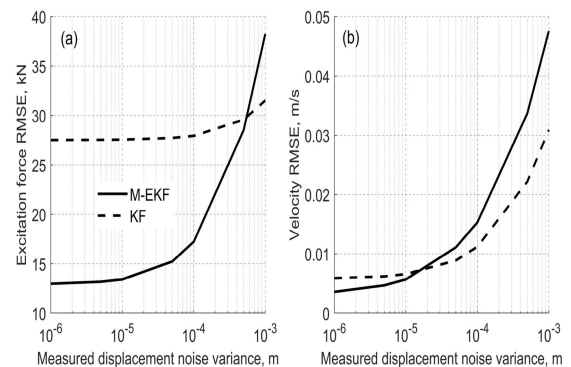


FIGURE 11. M-EKF and KF estimator performance under increasing displacement measurement noise variance: (a) RMSE of the excitation force estimate; (b) RMSE of the heave velocity estimate.

for signals with frequencies much higher than the rotating reference frame frequency. Therefore, regardless of the measurement noise characteristics, the noise will be filtered out by the $d-q$ transformation, rendering the E-EKF estimator to be immune to measurement noise.

Unlike the E-EKF estimator, the mechanical-based estimators (i.e., M-EKF and KF) are prone to noise contained in heave displacement measurements. A translational position sensor is utilized to measure the floater heave displacement. The underlying nominal measurement noise is modeled as white noise with zero mean and a variance of 1×10^{-6} m,

TABLE 2. E-EKF, M-EKF, and KF estimator performances in estimating the wave excitation force under three different loading scenarios.

Metric (unit)	Resistive Loading			Diode Rectifier			Boost Rectifier		
	KF	M-EKF	E-EKF	KF	M-EKF	E-EKF	KF	M-EKF	E-EKF
NMSE	0.7859	0.9083	0.9224	0.7781	0.9162	0.9321	0.7808	0.9171	0.9326
EB (kN)	-0.806	-0.6877	-0.7803	0.5693	0.1934	0.1946	0.5605	0.5328	0.5229
RMSE (kN)	31.1707	13.3522	11.3103	32.3137	12.2075	9.8971	31.9237	12.0782	9.8228
EEPE (%)	24.4901	6.1062	3.8961	37.7164	8.8751	5.5376	26.5932	5.6724	3.6884

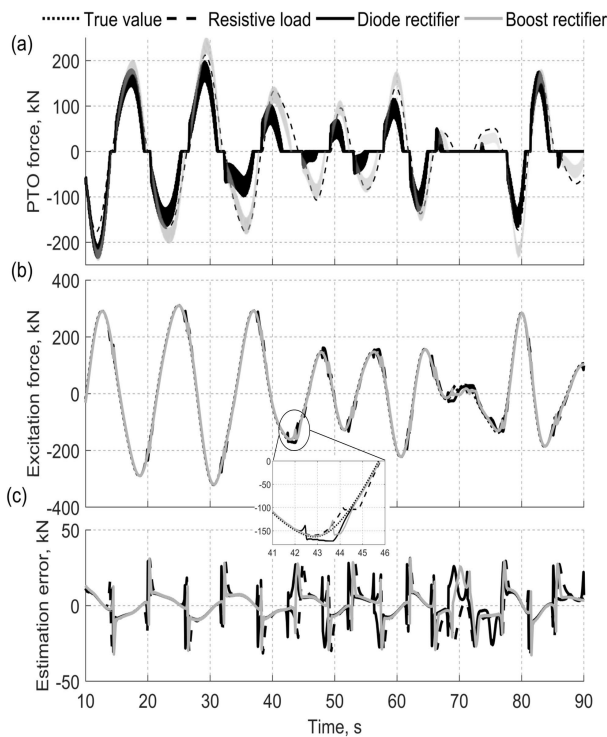


FIGURE 12. E-EKF estimator performance under different loading scenarios: (a) PTO electromagnetic force; (b) excitation force estimates; (c) estimation error.

indicating low noise contamination. The performance of both M-EKF and KF estimators under varying measurement noise variance is investigated and the results are shown in Fig. 11. It is clear that, as the noise variance increases, the M-EKF estimator performance in estimating the excitation force deteriorates, as shown in Fig. 11(a). The linearized KF estimator exhibited much better performance, being nearly immune to measurement noise up to variance levels of 1×10^{-4} m. Both estimators exhibited poor performance in estimating the floater velocity with increasing noise in the displacement measurement, as shown in Fig. 11(b).

E. EFFECT OF ELECTRIC LOADING SCENARIOS

To examine the performance of the developed state estimators under linear and nonlinear loading scenarios, three loading

scenarios are considered: three-phase resistive loading, three-phase diode rectifier loading, and three-phase boost rectifier loading, as depicted in Fig. 1. These loading scenarios generate an electromagnetic force with only a damping effect [14], [17]. A sea state of $H_s = 3$ m and $T_s = 12$ s is applied and the estimator’s goodness is assessed under the aforementioned loading scenarios. The three-phase resistance R_l is set to 5Ω , whereas the boost rectifier is loaded with a resistance of $R_{dc} = 50 \Omega$. Figure 12(a) showcases the resultant PTO force for the three adopted loading circuits. The corresponding excitation force estimate of the E-EKF estimator under different loading scenarios is plotted in Fig. 12(b). The E-EKF estimator produced accurate estimates of the excitation force with $NMSE > 0.92$ for all loading scenarios. The performance of the E-EKF estimator along with the other M-EKF and linearized KF estimators subject to different loading scenarios is summarized in Table 2.

V. CONCLUSION

An E-EKF estimator capable of estimating the wave excitation force and the floater’s heave displacement and velocity is proposed in this work. A holistic nonlinear wave-to-wire dynamic model was utilized to embed the possible nonlinear dynamics resulting from drag and friction force– in the framework of the estimator. The estimator offers a good balance between estimation accuracy and ease of implementation, only requiring real-time measurement of the three-phase PMLG stator currents. Using a one-sample delayed estimate of the floater displacement, the three-phase currents are transformed to the more noise-immune synchronous reference frame. Also, the excitation force estimate can be used to estimate the water surface velocity needed for computing the viscous drag force in real time. All the aforementioned measures assist in avoiding to need to use dedicated wave elevation measuring techniques, which helps in reducing the system’s costs. Another benefit of using electrical transducers (e.g., CTs) is the fact that they are more suitable for hardware redundancy, which in turn can be used in fault diagnosis and tolerance applications. One drawback of the proposed technique is that the quality of the measured current signals depends not only on the quality of the transducers used but also on the goodness of the designed estimator. More work needs to be done to further evaluate the effectiveness

of the proposed estimation technique, e.g., using it with sub-optimal amplitude and phase control strategies, in which much more aggressive linear and nonlinear dynamics are encountered.

APPENDIX I. WEC DESIGN PARAMETERS

A. HYDRODYNAMIC PARAMETERS

$$T_s = 1 \times 10^{-5} \text{ s}, m = 30189 \text{ kg}, \rho = 1025 \text{ kg/m}^3, \\ A_w = 19.64 \text{ m}^2, m_\infty = 28518 \text{ kg}, S_b = 197370 \text{ N/m}, \\ C_d = 1. A_r = \begin{pmatrix} -3.2914 & -7.9461 & -7.7067 & -4.2272 \\ 1 & 0 & 0 & 0 \\ 0 & 1 & 0 & 0 \\ 0 & 0 & 0 & 1 \end{pmatrix},$$

$$B_r = (1 \ 0 \ 0 \ 0)^T, \\ C_r = (14745 \ 52918 \ 41145 \ 0).$$

$$a_0 = 0.1271, a_1 = 1.631, a_2 = 7.566, a_3 = 9.093, a_4 = 20.21, \\ a_5 = 12.4, a_6 = 18.81, a_7 = 6.233, a_8 = 7.279, a_9 = 1.046, a_{10} = 1.$$

$$b_0 = -1.03 \times 10^{-12}, b_1 = 4.537 \times 10^5, b_2 = 7.712 \times 10^5, \\ b_3 = 1.465 \times 10^6, b_4 = 1.624 \times 10^6, b_5 = 1.48 \times 10^6, \\ b_6 = 1.182 \times 10^6, b_7 = 5.935 \times 10^5, b_8 = 3.549 \times 10^5, \\ b_9 = 8.216 \times 10^4, b_{10} = 3.711 \times 10^4.$$

B. POWER TAKE-OFF (PTO) SYSTEM PARAMETERS

$$S_{rs} = 60000 \text{ N/m}, F_n = 12000 \text{ N}, \mu_d = 1, \mu_v = 2, \mu_s = 2, \\ v_s = 1 \text{ m/s}, \alpha = 10, R_s = 2 \ \Omega, L_s = 25 \text{ mH}, \psi_{PM} = 19.8 \text{ Wb}, \\ p_w = 45 \text{ mm}, R_l = 5 \ \Omega, R_{dc} = 50 \ \Omega.$$

C. ESTIMATORS DESIGN PARAMETERS

$$Q_e = q'_e * q_e, \\ q_e = [1 \times 10^{-10}, 1 \times 10^{-10}, 1 \times 10^{-10}, 1 \times 10^{-10}, 1 \times 10^{-10}, \\ 1 \times 10^{-10}, 2 \times 10^4, 1 \times 10^{-2}, 1 \times 10^{-2}],$$

$$R_e = \text{diag}(r_e), \\ r_e = [1 \times 10^{-3}, 1 \times 10^{-3}, 1 \times 10^{-3}, 1 \times 10^{-3}, 1 \times 10^{-3}, 1 \times 10^{-3}, \\ 1 \times 10^{-3}, 1 \times 10^{-1}, 1 \times 10^{-2}],$$

$$Q_m = q'_m * q_m, \\ q_m = [1 \times 10^{-5}, 1 \times 10^{-5}, 1 \times 10^{-9}, 1 \times 10^{-9}, 1 \times 10^{-9}, 1 \times 10^{-9}, \\ 1 \times 10^{-9}, 1 \times 10^{10}],$$

$$R_m = \text{diag}(r_m), \\ r_m = [100, 1 \times 10^{-9}, 1 \times 10^{-9}, 1 \times 10^{-9}, 1 \times 10^{-9}, 1 \times 10^{-9}, \\ 1 \times 10^{-9}, 1 \times 10^{-9}],$$

$$Q_{ml} = q'_{ml} * q_{ml}, \\ q_{ml} = [1 \times 10^{-5}, 1 \times 10^{-5}, 1 \times 10^{-9}, 1 \times 10^{-9}, 1 \times 10^{-9}, 1 \times 10^{-9}, \\ 1 \times 10^{-9}, 5 \times 10^5],$$

$$R_{ml} = 200,$$

REFERENCES

- [1] J. Falnes, *Ocean Waves and Oscillating Systems*. Cambridge, U.K.: Cambridge Univ. Press, 2002.
- [2] T. Taghipoura, T. Perez, and T. Moan, "Hybrid frequency-time domain models for dynamic response analysis of marine structures," *Ocean Eng.*, vol. 35, pp. 685–705, May 2008.
- [3] WAMIT. (2019). *WAMIT User Manual Version 7.3*. Chestnut Hill, MA, USA. Accessed: Dec. 11, 2019. [Online]. Available: http://www.wamit.com/manualupdate/v73_manual.pdf
- [4] F. Fusco and J. V. Ringwood, "A simple and effective real-time controller for wave energy converters," *IEEE Trans. Sustain. Energy*, vol. 4, no. 1, pp. 21–30, Jan. 2013.

- [5] P. Kracht, S. Perez-Becker, J.-B. Richard, and B. Fischer, "Performance improvement of a point absorber wave energy converter by application of an observer-based control: Results from wave tank testing," *IEEE Trans. Ind. Appl.*, vol. 51, no. 4, pp. 3426–3434, Jul. 2015.
- [6] O. Abdelkhalik, S. Zou, R. Robinett, G. Bacelli, and D. Wilson, "Estimation of excitation forces for wave energy converters control using pressure measurements," *Int. J. Control*, vol. 90, no. 8, pp. 1793–1805, Aug. 2017.
- [7] B. Guo, R. J. Patton, S. Jin, and J. Lan, "Numerical and experimental studies of excitation force approximation for wave energy conversion," *Renew. Energy*, vol. 125, pp. 877–889, Sep. 2018.
- [8] H.-N. Nguyen and P. Tona, "Wave excitation force estimation for wave energy converters of the point-absorber type," *IEEE Trans. Control Syst. Technol.*, vol. 26, no. 6, pp. 2173–2181, Nov. 2018.
- [9] B. Ling and B. Batten, "Real time estimation and prediction of wave excitation forces on a heaving body," in *Proc. ASME 34th Int. Conf. Ocean, Offshore Arctic Eng.*, 2015, pp. 1–10.
- [10] Y. Pena-Sanchez, M. Garcia-Abril, F. Paparella, and J. V. Ringwood, "Estimation and forecasting of excitation force for arrays of wave energy devices," *IEEE Trans. Sustain. Energy*, vol. 9, no. 4, pp. 1672–1680, Oct. 2018.
- [11] M. Abdelrahman and R. Patton, "Robust control of a wave energy converter with soft sensing of wave excitation force," in *Proc. 12th Eur. Wave Tidal Energy Conf.*, 2017, pp. 974–1–974-10.
- [12] M. Jama, A. Wahyudie, and H. Noura, "Robust predictive control for heaving wave energy converters," *Control Eng. Pract.*, vol. 77, pp. 138–149, Aug. 2018.
- [13] Z. Ballard and B. P. Mann, "Two-dimensional nonlinear analysis of an untethered spherical buoy due to wave loading," *J. Comput. Nonlinear Dyn.*, vol. 8, no. 4, Oct. 2013, Art. no. 041019.
- [14] M. Jama and A. Wahyudie, "Online damping strategy for controlling heaving wave energy converters using three-phase bridge boost rectifier," *IEEE Access*, vol. 5, pp. 7682–7691, 2017.
- [15] I. Boldea and S. Nasar, *Linear Electric Actuators and Generators*. Cambridge, U.K.: Cambridge Univ. Press, 1997.
- [16] S. Sul, *Control of Electric Machine Drive Systems*. Hoboken, NJ, USA: Wiley, 2011.
- [17] A. Wahyudie and M. A. Jama, "Perspectives on damping strategy for heaving wave energy converters," *IEEE Access*, vol. 5, pp. 22224–22233, 2017.
- [18] L. Chang and A. Lee, "Design of nonlinear controller for bi-axial inverted pendulum system," *IET Control Theory Appl.*, vol. 1, no. 4, pp. 979–986, 2007.
- [19] S. Andersson, A. Söderberg, and S. Björklund, "Friction models for sliding dry, boundary and mixed lubricated contacts," *Tribol. Int.*, vol. 40, no. 4, pp. 580–587, Apr. 2007.
- [20] D. Simon, *Optimal State Estimation*. Hoboken, NJ, USA: Wiley, 2006.



MOHAMMED JAMA was born in Al Ain, UAE, in 1984. He received the B.S. and Ph.D. degrees in electrical engineering from United Arab Emirates (UAE) University, Al Ain, in 2009 and 2015, respectively. From 2015 to 2018, he was a Postdoctoral Fellow of the Department of Electrical Engineering, UAE University, where he also served as an Adjunct Faculty Member. He is currently a Research Fellow of the Emirates Centre of Energy and Environment Research (ECEER), UAE University. His research interests include modeling and control of renewable energy systems, such as solar energy, wind energy, and marine energy, distributed generation, and energy storage systems.



ADDY WAHYUDIE received the B.S. degree in electrical engineering (majoring in control systems) from Gadjah Mada University, Indonesia, in 2002, the M.Eng. degree in electrical engineering from Chulalongkorn University, Thailand, in 2005, and the D.Eng. degree in electrical engineering from Kyushu University, Japan, in 2010. From 2005 to 2011, he was a Lecturer with the Department of Electrical Engineering, Gadjah Mada University. In 2011, he joined United Arab Emirates (UAE) University as an Assistant Professor. He is currently an Associate Professor with the Department of Electrical Engineering, UAE University. His research interests include control systems theory (robust control, intelligent control, and model predictive control) and its applications in electromechanical and renewable energy systems (marine energy).



SAAD MEKHILEF (Senior Member, IEEE) received the B.Eng. degree in electrical engineering from the University of Sétif, Sétif, Algeria, in 1995, and the master's degree in engineering science and the Ph.D. degree in electrical engineering from the University of Malaya, Kuala Lumpur, Malaysia, in 1998 and 2003, respectively. He is currently a Professor and the Director of the Power Electronics and Renewable Energy Research Laboratory, Department of Electrical Engineering, University of Malaya. He is also the Dean of the Faculty of Engineering, University of Malaya. He is also a Distinguished Adjunct Professor with the School of Software and Electrical Engineering, Faculty of Science, Engineering, and Technology, Swinburne University of Technology, Melbourne, Australia. He has authored or coauthored more than 450 publications in international journals and conference proceedings. His current research interests include power converter topologies, the control of power converters, renewable energy, and energy efficiency.

...